Habitability of Martian Noachian Hydrothermal Systems as Constrained by a Terrestrial Analog on the Colorado Plateau

Jake R. Crandall[1,2] , Justin Filiberto[3] , Nicholas Castle[3,4], Sally L. Potter-McIntyre[2], Susanne P. Schwenzer[5] ,
Karen Olsson-Francis[5], and Scott Perl[6]

[1] Eastern Illinois University, Department of Geology & Geography, 600 Lincoln Avenue, Charleston, IL 61920, USA
[2] Southern Illinois University, School of Earth Systems and Sustainability, Department of Geology, 1259 Lincoln Drive, Carbondale, IL 62901, USA
[3] Lunar and Planetary Institute, USRA, 3600 Bay Area Boulevard, Houston, TX 77058, USA
[4] Now at Planetary Science Institute, 1700 East Fort Lowell, Suite 106, Tucson, AZ 85719, USA
[5] AstrobiologyOU, EEES, The Open University, Walton Hall, Milton Keynes MK7 6AA, UK
[6] Jet Propulsion Laboratory, California Institute of Technology, 4800 Oak Grove Drive, Pasadena, CA 91109, USA
Received 2021 February 9; revised 2021 May 13; accepted 2021 May 13; published 2021 July 29

Abstract

Volcanic features and impact craters are ubiquitous features on Mars, and hydrothermal systems associated with the production of these features should have been abundant in Mars's early history. These hydrothermal systems represent potentially habitable environments and are therefore a high priority for continued investigations of the Martian crust. Here we present a Mars analog study where basaltic magma intruded water-bearing sediments to produce a high-temperature (as high as ~700°C) hydrothermal system, which we use to constrain the potential habitability of similar systems on Mars via mineralogy and geochemistry including S, C, and O isotopic systematics. Our analog site suggests evidence for a habitable environment once the system cooled below 120°C and the potential presence of microbial activity based on the combination of dolomite and C-isotopic systems in the same sample. These findings highlight the importance of future missions to investigate the interface of sediments with magmas and/or late-stage impact melts where microbial life may have taken hold when temperature conditions allowed.

Unified Astronomy Thesaurus concepts: Mars (1007)

1. Introduction

High-temperature hydrothermal systems associated with both volcanic activity and impact processes should have been abundant during the Noachian (Newsom 1980; Farmer 1996; Abramov & Kring 2005; Carr & Head 2010; Rodríguez & Van Bergen 2016). Here we define high-temperature hydrothermal systems as having a peak fluid temperature ≫100°C to distinguish from those systems near or below the boiling temperature of water at Earth's surface pressure. Potential microbial activity may have used the energy and nutrients from these systems in a similar manner to hydrothermal systems on Earth (e.g., Rothschild & Mancinelli 2001; DasSarma 2006; Cockell et al. 2016; Rodríguez & Van Bergen 2016). Thus, it is important to understand those systems through the investigation of terrestrial analogs. As one such analog, especially applicable to Jezero and Gusev Craters, Costello et al. (2020) previously investigated a mafic dike in the Entrada Sandstone (an iron-cemented fine-grained red silty sandstone) of the San Rafael Swell (Utah, USA) that was hydrothermally altered from contact with reservoir fluids as it was emplaced. This previous work specifically investigated the effects of hydrothermal alteration on the mineralogy and bulk chemistry of the dike itself. Here we build on this work to investigate the effects of the hydrothermal system on the mineralogy and geochemistry including sulfur, carbon, and oxygen isotopic systematics of the country rock. Further, we have reanalyzed previously studied altered mafic dike samples (Costello et al. 2020) for

sulfur, carbon, and oxygen isotopes. Combining the geochemical, mineralogic, and isotopic data, we constrain habitability conditions during hydrothermal systems in the ancient Martian Noachian crust.

During the Noachian, the Martian crust was a dynamic environment with both volcanism and meteorite impacts churning and modifying the newly formed and evolving crust (e.g., Carr 1980; Strom et al. 1992; Wilson & Head 1994; Carr & Head 2010). Water was likely present, stable, and presumably flowing on the surface (e.g., Carr 1980; Clifford & Parker 2001; Taylor & McLennan 2009; Carr & Head 2010; Ehlmann & Mustard 2012; Williams et al. 2013; Lasue et al. 2019). Based on topographic features, there may have even been an ocean in the northern hemisphere (e.g., Malin & Edgett 1999), though this remains heavily debated (e.g., Carr & Head 2003; Andrews-Hanna et al. 2008; Stanley et al. 2008; Leone 2020). Interactions between these diverse environments should have occurred—impacts and volcanism would have provided enough heat to the crust to mobilize fluids, sourced from groundwater and/or brines, ground ice or cryosphere/ice melt, or bound in hydrated minerals (Perl & Baxter 2020). This interaction would have produced contact metamorphism with the country rock and generated a hydrothermal system with any fluids present, similar to processes that are well documented on Earth (Griffiths 2000; Hochstein & Browne 2000; Osinski et al. 2001; Abramov & Kring 2005, 2007; Pirajno & Van Kranendonk 2005; Schwenzer et al. 2012b; Osinski et al. 2013; Rodríguez & Van Bergen 2016; Turner et al. 2016). On Earth, such hydrothermal systems represent habitable environments and may be where life began (Farmer 1996; Shock 1996; Shock et al. 1998; Nisbet & Sleep 2001; Pirajno & Van Kranendonk 2005; Cockell 2006; Sapers et al. 2009; Kring et al. 2020). Due to this

potential for habitability, and perhaps even the origin of life, hydrothermally altered crust has been a top priority for investigations of the Martian crust (e.g., Schulze-Makuch et al. 2007).

However, Mars has transitioned to a drier climate with the loss of the majority of the atmosphere, diminishing the possibility of large-scale hydrothermal systems during the Amazonian period (e.g., Jakosky & Phillips 2001; Bibring et al. 2006; Carr & Head 2010; Turner et al. 2016). Therefore, in order to study such ancient hydrothermal systems, proxies must be investigated, such as the remnant mineralogy of extinct hydrothermal systems. Unlike Earth's crust, which is dominated by felsic rocks and siliceous minerals, the Martian crust is largely basaltic (e.g., McSween & Treiman 1998; McSween et al. 2003; Taylor et al. 2010; Filiberto 2017; Udry et al. 2020), and secondary minerals produced during alteration will be reflective of this low-Si–Al and high-Fe–Mg protolith (e.g., Zolotov & Mironenko 2007; Schwenzer & Kring 2013; Semprich et al. 2019). Secondary minerals have been observed from orbit, by ground-based missions, and in Martian meteorites (e.g., Ehlmann & Edwards 2014; Rampe et al. 2017, 2020a; Bridges et al. 2019; Filiberto & Schwenzer 2019); however, finding evidence of high-temperature hydrothermal systems and contact metamorphism from orbit has been met with limited success (e.g., Crandall et al. 2021; Ehlmann et al. 2011; Viviano et al. 2013; Viviano-Beck et al. 2014; McSween et al. 2015; Semprich et al. 2019). From orbit, only limited exposures of magmatic-hydrothermal alteration activity have been suggested based on mineralogy and chemistry: for example, at Nili Patera caldera (Skok et al. 2010), at Valles Marineris Chasma (Milliken et al. 2008; Thollot et al. 2012), and potentially near volcanic terrains, specifically the Medusae Fossae Formation (Keller et al. 2006; Filiberto et al. 2019). The best-explored example of a magmatic-hydrothermal system (Ruff & Farmer 2016; Ruff et al. 2020) is in Gusev Crater, which was investigated in detail by the Mars Exploration Rover (MER) Spirit but was not detected from orbital investigations (Squyres et al. 2008; Yen et al. 2008; Ruff et al. 2011; Filiberto & Schwenzer 2013; Schmidt et al. 2014). Furthermore, evidence for impact-generated hydrothermal systems has been suggested based on the mineralogy detected from orbit and in situ within the Noachian and Hesperian, but not Amazonian, crust (e.g., Osinski et al. 2013; Arvidson et al. 2014; Turner et al. 2016; Schröder & Schwenzer 2017). However, the chemical and mineralogical signatures of such habitable hydrothermal systems on Mars are not well constrained. Terrestrial analogs are needed to characterize the specific mineralogical and chemical changes in order to find and explore such systems in the Martian crust.

Therefore, here we report the mineralogy, geochemistry, and S, C, and O isotopic systematics of such a Mars analog system: an altered mafic dike and the surrounding metamorphic contact zone showing evidence for high-temperature fluid mobility. Our results will be used to constrain the potential alteration mineralogy present in the Early Martian crust from high-temperature hydrothermal systems and the potential habitability of such systems.

2. Field Site and Previous Work

During the 2017 field season, samples were collected from our investigation site approximately 60 km SW of Green River on the San Rafael Swell, Utah, USA, where a 22 Ma mafic dike
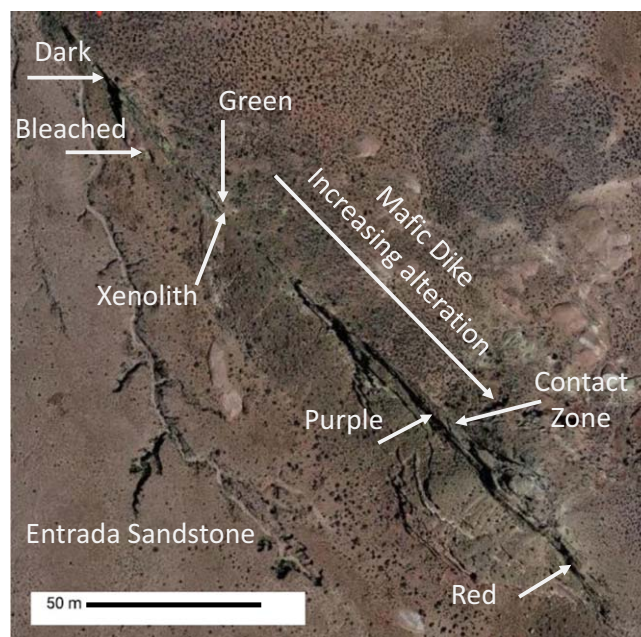

Figure 1. Google Maps view of the dike and surrounding area of our field site. Arrows point out the approximate locations where each sample was collected.

intruded the Entrada Sandstone (N38°31′.116 W110°26′.656)—the Robbers Roost Dike (Figure 1), a light rare earth element (LREE) enriched olivine-phlogopite-lamproite (Wannamaker et al. 2000). The dike intruded though the Jurassic Entrada Sandstone, an iron-cemented fine-grained red silty sandstone deposited in an eolian to tidal environment (Wright et al. 1979; O'Sullivan 1981; Crabaugh & Kocurek 1993).

Costello et al. (2020) previously reported the effects of the hydrothermal alteration on the mineralogical changes of the dike itself (Figure 2). This work showed that the hydrothermal fluids removed Si and K from the dike and added S, Fe, Ca, and possibly Mg. All samples contain calcite, hematite, and kaolinite, with most samples containing minor anatase, barite, halite, and dolomite. Based on a comparison of the combination of alteration mineralogy and changes in bulk chemistry along the dike with thermochemical models (Filiberto & Schwenzer 2013), alteration of the mafic dike records conditions up to ~200°C and a near-neutral pH CO_2-bearing fluid. However, this work did not investigate the metamorphic reactions within the Entrada Sandstone or the bleached zones peripheral to the dike, which more directly record the composition and temperature of the hydrothermal system. Further, Costello et al. (2020) did not investigate the effects of the hydrothermal system on isotopic systematics, which can be used to further constrain the habitability of the system. Therefore, here we will build on this previous work to investigate the mineralogical changes associated with the surrounding "baked contact zone" of the Entrada Sandstone, as well as bleached fractures distal to the dike. Note: we use the term "bleached" to mean sandstone with primary iron-oxide cement removed as per the extensive literature on iron diagenesis (e.g., Beitler et al. 2003, 2005; Chan et al. 2004; Parry et al. 2004; Potter & Chan 2011). Bleached refers to the color and not the oxidation reaction.

An important caveat to this work is that quartz sandstones have not been detected on Mars and are not likely, as the Martian crust is dominated by basaltic and not granitic compositions and minerals (e.g., McSween & Treiman 1998; McSween et al. 2003, 2009, 2015; Taylor et al. 2010;

Figure 2. Darkest, least altered portion of the dike (dark gray) in contact with the Entrada Sandstone. The dike is approximately 30 cm in thickness, with the contact zone on either side also approximately 30 cm thick. The contact zone here is yellow in color vs. the unaltered Entrada (float and shown distal to the dike in this image) being redder in color. This shows that the contact zone is more resilient to weathering than the dike itself or the surrounding unaltered Entrada Sandstone.

Figure 3. Contact zone with the red altered portion of the dike. This is specifically where sample 2 was taken. The contact zone here is approximately 20 cm across.

Filiberto 2017; Udry et al. 2020). This analog, however, allows a focus on magma interaction with groundwater in a porous sandstone and the mineralogy, geochemistry, and isotopic systematics produced and affected by the hydrothermal system. Sandstone and other sedimentary rocks dominate the surface lithology of Mars (e.g., Rogers et al. 2018); therefore, it is vital to investigate the habitability of hydrothermal environments established in sand, silt, and mudstone. Results from this work can be translated to Martian environments through thermo-chemical modeling (e.g., Baharier et al. 2021). Therefore, this work is applicable to such sedimentary systems on Mars to constrain the habitability and mineralogical changes associated with high-temperature hydrothermal activity. Further, since the Entrada is an iron-cemented sandstone, the system contains some iron, which could mimic iron added to the system from an iron-rich Martian crust (Taylor et al. 2006, 2010; McSween et al. 2009; Taylor & McLennan 2009). This added iron from the surrounding system could have provided nutrient sources for potential biological activity (e.g., Kostka et al. 2002; Nixon et al. 2012).

3. Samples

In order to provide sufficient material for multiple analyses, as well as little contamination between samples, large samples (typically 20 cm in length or longer) were collected at each site where material was available (Figure 1). The samples were collected in sample bags (either cloth or plastic) before being split using a rock splitter and processed in the laboratory. Fresh interior samples were targeted for analyses in order to avoid surface contamination. Splits of each sample were made into thin sections for optical petrographic descriptions (Spectrum Petrographics, Inc., in Vancouver, WA, USA). Sample numbers are provided in parentheses and are consistent with the figures and supplemental tables (Crandall 2021).

Entrada sandstone unaffected by magmatic-hydrothermal activity. At the entrance to the Flat Tops area (38°32′18″.6N 110°29′26″.3W; approximately 10 km from the dike), a grab sample of Entrada Sandstone (sample 34) that was not affected by the magmatic intrusion was taken for comparison.

Altered dike samples. Samples from Costello et al. (2020) that have been analyzed and discussed here focus on alteration of the mafic dike (Figures 1, 2). Here we will review the important aspects of these samples as applicable to this study, but for a full description of the samples, their mineralogy, and bulk geochemistry see Costello et al. (2020). The dike is variably altered and can be separated into four distinct zones based on color of the dike, which corresponds to mineralogical changes: darkest and least altered (sample 16), green and friable (sample 31), dark purple (sample 11), and the most altered bright red (sample 5). Mineralogically, all samples contain primary phologopite, with secondary calcite, hematite, and kaolinite. The red and dark-purple samples also contain minor anatase, barite, halite, and dolomite. Specifically, the number of alteration minerals increases with alteration. The green and most friable sample was dominated by carbonates.

Metamorphosed samples. A large piece of the Entrada Sandstone (sample 2) in direct contact with the most altered portion of the dike (sample 5—red) was taken (Figures 1, 3). Three subsamples were selected proximal to the contact (sample 2D), in the middle of the sample (2G), and along the outer edge (sample 2E). Only the proximal sample was made into a thin section. Samples were collected from a bleached fracture zone that ran parallel to the main dike (Figures 1, 4). The sample was then split for analyses of the bulk sample (sample 30 Bulk) and the portion away from the fracture portion (sample 30 Proximal). Further, on the open face of the
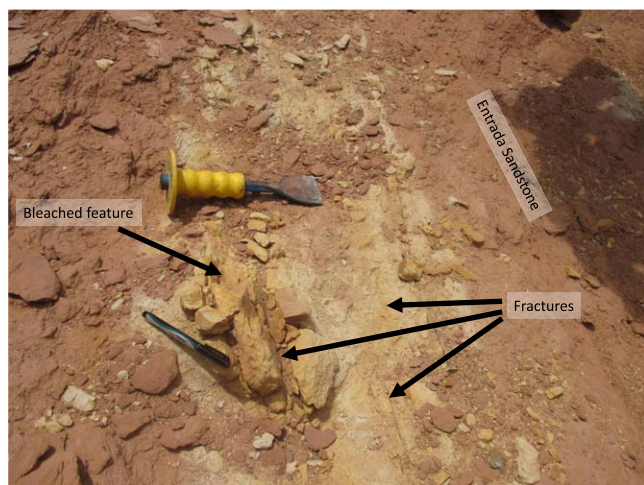
Figure 4. The bleached fracture zone showing the discoloration of the Entrada Sandstone from red (unaltered) to yellow and finally nearly white at the fracture. This is where sample 30 was taken. The chisel for scale is approximately 20 cm in length.

Figure 5. Xenolith sample 27 showing a small block of the Entrada Sandstone incorporated into the dike during emplacement. Finger for scale.

fracture were large crystals, which were handpicked from the bulk sample (sample 30 Vein).

Finally, sample 27 is a piece of the Entrada Sandstone that was incorporated into the dark portion dike as it was emplaced (Figures 1, 5). The sample is variable in color from red, which is consistent with the unaltered Entrada Sandstone, to white, consistent with the bleached zone. This sample was analyzed for mineralogy based on three splits: host dike, xenolith, and interfingered containing both xenolithic and dike material. This sample was not analyzed for bulk chemistry or isotopes, as even the xenolithic material contained portions of the dike.

4. Analytical Methods

Samples of the contact zone, the unaltered Entrada Sandstone, and a piece of the Entrada Sandstone incorporated into the dike as xenolithic material were analyzed for mineralogy by X-ray diffraction (XRD) in the Astromaterials Research and Exploration Sciences Division (ARES) XRD laboratory at NASA's Johnson Space Center (JSC). Chips were collected from each sample and then ground under acetone using either a mortar and pestle or a ball grinder, both made from alumina. Sample 30 Vein, where dissolution was a concern, was ground dry in a mortar and pestle. Samples were sieved to ensure homogeneous grinding, with coarse fractions reground until all material passed through a 45 μm sieve. All grinding equipment was cleaned by washing and replicate grinding of a pure quartz sand before and after each sample. Samples were analyzed using a Rigaku MiniFlex benchtop X-ray diffractometer with a Co Kα X-ray source over a range of 2°–80° 2θ. The scan step size was 0.02° 2θ with a 0.24 s dwell per step. Mineral identification and quantification were performed using Rietveld refinement in the Jade 10 software package (Materials Data Incorporated, Livermore, CA). Quantitative mineralogy is reported in Supplemental Table 1 (Crandall 2021). The same samples were examined using optical microscopy to confirm mineral identification and document microtextures. Based on the mineralogical results, along with the amount of sample material, splits of all samples were sent for bulk chemical analyses, except the samples of the xenolithic and adjacent material (sample 27).
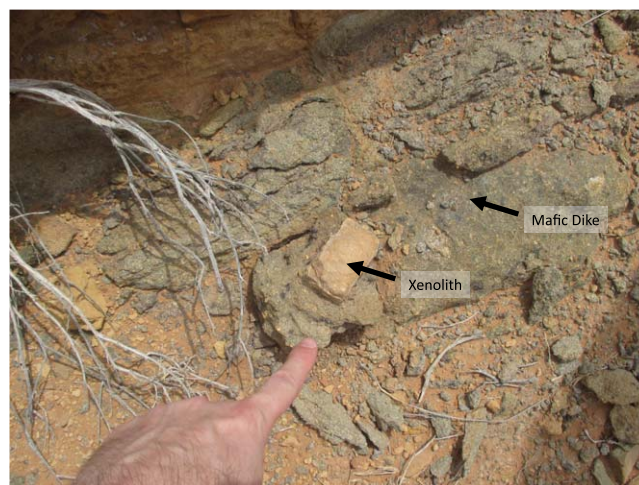
Analyses for bulk chemistry (major and trace elements) were performed for the surrounding contact zone and one unaltered sample of the Entrada Sandstone (Activation Laboratories, Ltd., in Ancaster, Ontario, Canada) for comparison by Elements Fusion Inductively Coupled Plasma-Optical Emission Spectrometry (ICP-OES) and Inductively Coupled Plasma Mass Spectrometry (ICP-MS), respectively. Oxygen, sulfur, and carbon isotopic measurements of the contact zone, unaltered Entrada Sandstone, and the altered dike samples from Costello et al. (2020) were also analyzed by Activation Laboratories. See archived data, which include quality control, for more information in the full report from Activation Laboratories (Supplemental Tables 1 and 2; Crandall 2021).

5. Results

Unaltered Entrada Sandstone. The unaltered Entrada Sandstone is dominated by quartz, with sanidine, muscovite, and albite (Table 1; Supplemental Table 2; Crandall 2021) and trace/minor enstatite, dolomite, gypsum, kaolinite, rutile, and hematite. Consistent with the mineralogy, geochemically, it is dominated by SiO_2 with abundant (>1 wt%) Al_2O_3, MgO, CaO, K_2O, and Na_2O. It has 4.03% LOI (loss on ignition), presumably representative of CO_2 that was released from calcite and dolomite and H_2O from kaolinite (Figure 6). It is enriched in trace elements and has a small negative europium anomaly. It has $-11.2‰$ $\delta^{18}O$, $-2.2‰$ $\delta^{13}C$, and $22‰$ $\delta^{34}S$ (Supplemental Table 1; Crandall 2021).

Mineralogy. Here we focus on the dominant mineralogy of each sample (Table 1; Supplemental Table 2; Crandall 2021), as well as trace minerals that inform alteration conditions; the low abundance minerals dominate the changes from sample to sample. Further, these trace minerals typically record the specific temperatures or fluid compositions during alteration. The metamorphosed contact zone (sample 2) is dominated by quartz, sanidine, calcite, dolomite, and albite (Table 1; Supplemental Table 2; Crandall 2021). The most significant change with increased distance from the contact is that the proportion of quartz changes from 59 to 73 wt%, which corresponds to the proportion of carbonates changing from 16% to 7% (dominated by calcite for the inner and outer portions, but interestingly dolomite for the middle sample). This is consistent with optical petrographic analyses showing

Table 1
Major Element Bulk Chemistry, S, C, and Isotopes, and Key Mineralogy

	34 Unaffected Entrada	30 Vein	30 Proximal	30 Bulk	2 G Middle	2 D Inside	2 E Outside	27 Xenolith	11 Purple	5 Red	16 Dark	31 Green
SiO_2	75.42	7.43	79.29	82.24	78.79	72.3	83.7		*27.6*	*26.1*	*34.8*	*32.8*
Al_2O_3	7.72	1.15	6.86	6.63	4.4	4.22	4.65		*16.9*	*14.0*	*14.7*	*16.6*
$Fe_2O_3(T)$	1.79	0.5	1.24	1.21	1.44	0.73	1.24		*29.1*	*25.8*	*22.1*	*5.5*
MnO	0.049	0.083	0.026	0.027	0.024	0.037	0.027		*0.2*	*0.2*	*0.3*	*0.3*
MgO	1.64	0.27	0.78	0.83	1.91	0.21	0.26		*3.3*	*6.5*	*3.8*	*1.3*
CaO	5.61	21.85	1.56	1.29	3.64	10.78	4.42		*12.4*	*17.3*	*11.6*	*28.7*
Na_2O	1.22	0.09	0.9	0.9	0.49	0.36	0.32		*0.9*	*1.4*	*0.0*	*0.0*
K_2O	2.43	0.45	3.92	3.19	2.88	2.74	2.23		*1.9*	*1.9*	*4.4*	*4.1*
TiO_2	0.4	0.033	0.243	0.247	0.196	0.139	0.14		*5.3*	*4.8*	*5.7*	*7.4*
P_2O_5	0.14	0.03	0.07	0.08	0.05	0.04	0.05		*2.3*	*2.2*	*2.6*	*3.2*
LOI	4.02	13.36	2.06	1.82	5.46	7.21	1.7					
Total	100.4	45.25	96.95	98.46	99.3	98.76	98.73		*100.00*	*100.00*	*100.00*	*100.00*

b.d. - below detection limit; LOI—Loss on ignition; $Fe_2O_3(T)$ = Total iron = $FeO + Fe_2O_3$

Bulk Geochem and Mineralogy Data for Altered Dike in Italics from Costello et al. (2020). Data have been renormalized to wt% oxides, and elements not analyzed here have been removed.

	34 Unaffected Entrada	30 Vein	30 Proximal	30 Bulk	2 G Middle	2 D Inside	2 E Outside	27 Xenolith	11 Purple	5 Red	16 Dark	31 Green
d18O—	−11.2	−14.4	−9.7	−8.6	−16.9	−17.2	−15.1		−13.4	−13.6	−11.9	−9.2
d13C	−2.2	−5.1	−2.5	−2.2	−0.7	−5.3	−3.2		−4.1	−4.1	−4.8	−4
d34S	22	15	16	12.4	16	13.7	24.2		15.4	10.5	13.3	16.1

Key Mineralogy (for full mineralogy and mineral percents see supplementary information)

	34 Unaffected Entrada	30 Vein	30 Proximal	30 Bulk	2 G Middle	2 D Inside	2 E Outside	27 Xenolith	11 Purple	5 Red	16 Dark	31 Green
	Quartz	Quartz	Quartz	Quartz	Quartz	Quartz	Quartz	Quartz	*Phlogopite*	*Phlogopite*	*Phlogopite*	*Phlogopite*
	Sanidine	Sanidine	Sanidine	Sanidine	Sanidine	Sanidine	Sanidine	Sanidine	*Sanidine*	*Sanidine*	*Sanidine*	*Hematite*
	Albite	Andesine	Albite	Albite	Albite	Albite	Albite	Andesine	*Hematite*	*Hematite*	*Hematite*	*Calcite*
	Caclite	Calcite	Dolomite	Calcite	Dolomite	Calcite	Calcite	Calcite	*Calcite*	*Calcite*	*Calcite*	*Kaolinite*
	Dolomite	Celestine		Dolomite				Dolomite	*Dolomite*	*Dolomite*	*Kaolinite*	
	Muscovite	Marialite		Muscovite				Kaolinite	*Kaolinite*	*Kaolinite*	*Gypsum*	
	Kaolinite							Tridymite	*Halite*	*Halite*		
								Nitratine		*Goethite*		
										Gypsum		

Note. Trace and minor element and detailed mineralogy (including mineral percentages) in supplementary materials archived on FigShare.
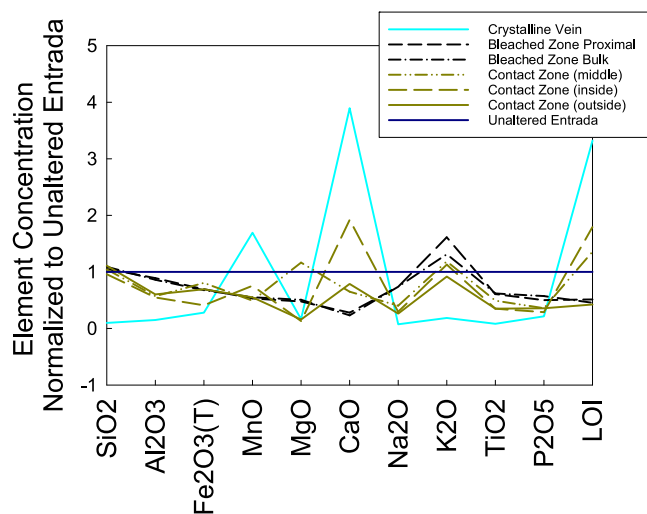
Figure 6. Bulk rock chemistry from each zone normalized to the unaltered Entrada Sandstone to display element mobility during alteration. Values less than 1 indicate elements that have been depleted compared with the unaltered sample and therefore were removed from the system during alteration, whereas values greater than 1 indicate elements that are enriched compared to the unaltered sample and are therefore added to the bulk chemistry of the system during alteration.

highly variable and higher amounts of carbonate (calcite or dolomite) cement than the unaltered entrada (sample 34) (Figure 8).

Similar to the baked contact zone, the xenolith (sample 27) is dominated by quartz (48%), but with almost 30% calcite and minor dolomite. Two minor minerals of note in the xenolithic material are tridymite and nitratine ($NaNO_3$). Nitratine is found to be ubiquitous in samples from our other Mars analog field site in the area (Crandall et al. 2021). The ubiquity of nitratine in desert samples should not be surprising since it is common in extremely dry climates (e.g., Cheng et al. 2016; Melchiorre et al. 2018) and interestingly has been also detected at Gale Crater by Mars Science laboratory Curiosity (e.g., Stern et al. 2015). Petrographically, the xenolith sample shows evidence of both carbonate replacement and deformation of primary minerals (Figure 7).

Away from the dike, the bleached zone (sample 30) is dominated by quartz but has almost no calcite and instead is dominated by sanidine and albite. Finally, in the bleached zone there were large crystals that grew on a fracture zone, which were removed from the bulk and measured separately (hereafter called the crystalline vein). This split of crystalline vein contains almost no quartz (likely the small amount analyzed is from contamination from the bulk; Table 1; Supplemental Table 1; Crandall 2021) but instead is dominated by radial bladed crystals of calcite, celestine, and marialite (Figure 7).

Geochemistry. Bulk geochemical changes are consistent with the mineralogical changes (Figure 6). For the baked contact (sample 2) zones, the chemistry is similar to the unaltered bulk chemistry. The only substantial changes are associated with carbonate stability—Ca, Mg, and LOI. These all correlate with the percent of calcite and dolomite in the XRD analyses. The decrease in sodium, titanium, and phosphorus in the unaltered versus altered samples suggests removal of these elements possibly during metamorphism and subsequent hydrothermal activity. There is a decrease in iron with increasing alteration across the baked zone, but the concentration of Fe does not decrease consistently with distance from the dike. Aluminum decreases substantially (by almost half), which could be due to the destabilization of feldspar consistent with the decrease in sodium; however, no accompanying change in potassium was observed. Silica shows a slight increase, which may be due to silica removal from the mafic dike and subsequent reprecipitation in the surrounding country rock as described previously by Costello et al. (2020), or due to the removal of other elements, including carbon. The bleached zone (sample 30) has similar bulk chemistry to the contact zone next to the dike. The crystal vein significantly differs in its bulk composition from the unaltered Entrada Sandstone or the contact or bleached zones, which is consistent with the differences in mineralogy between these samples, with the crystalline material containing relatively low silica but high calcium. Furthermore, the sum of all oxides is low, suggesting missing elements such as sulfur, carbon, and/or chlorine (Table 1; Supplemental Table 1; Crandall 2021), which would be needed in the bulk chemistry to be consistent with the mineralogy calcite, celestine, and marialite.

The unaltered Entrada Sandstone (sample 34) shows the highest REE concentrations of all samples analyzed (Figure 8). The bleached zone (sample 30) and contact zone (sample 2) have similar REE patterns to the unaltered sandstone. However, the crystalline vein material (sample 30 vein) displays a very different pattern—it is LREE enriched and has a stronger europium anomaly compared with the bulk. Sample 2D in the contact zone (the direct contact with the mafic dike) has a similar pattern to the crystalline material even though its mineralogy differs markedly, and its bulk major elements are consistent with the other bleached and baked zones rather than the vein material.

Isotopes. The top panel of Figure 9 compares the oxygen and carbon isotopes of each sample. Interestingly, the samples of the Entrada Sandstone at the contact (sample 2) are distinct from any other analyzed sample. They have relatively uniform negative oxygen isotopes (-15 to $-17‰$) and a range in carbon isotopes (-0.7 to $-5.3‰$). The contact inside and closest to the dike has values for $\delta^{13}C$ of $-5.3‰$ and $\delta^{18}O$ of $-17.2‰$, which are the most similar to the dike that ranges from -4.0 to $-4.8‰$ for $\delta^{13}C$ and from -10.5 to $-16.1‰$ for $\delta^{18}O$. Although most of the Entrada Sandstone values lie between the dike values and the unaltered sample ($\delta^{13}C = -2.2‰$; $\delta^{18}O = -11.2‰$), the outside and middle portions of the baked zone do not follow this pattern. The middle sample has a $\delta13C$ value of $0.7‰$ and a $\delta^{18}O$ value of -16.9, and the outside sample has a $\delta^{13}C$ value of $3.2‰$ and a $\delta^{18}O$ value of $-15.1‰$. The two bleached zone samples (sample 30, bulk and proximal) show values of $-2.2‰$ and $-2.5‰$ for $\delta^{13}C$ and -8.6 and $9.7‰$ for $\delta^{18}O$ (bulk and proximal, respectively) that are similar to the unaltered Entrada Sandstone sample (34) with $\delta^{13}C$ of $-2.2‰$ and $\delta^{18}O$ values of $-11.2‰$, suggesting that bleaching does not significantly affect oxygen and carbon isotopes. The crystalline vein material, however, has $\delta^{13}C = -5.1‰$ and $\delta^{18}O = -14.4‰$ and is similar to but slightly lighter than the dike samples—especially the dark or least altered samples.

The outside sample of the contact zone returned sulfur isotopes ($\delta34S = +24.2‰$) on par with the unaltered Entrada Sandstone ($\delta34S = +22‰$); however, the rest of the samples, regardless of bulk chemistry or mineralogy, have nearly constant sulfur isotopic composition (14.2 ± 1.9 $\delta^{34}S$) (Figure 9, bottom panel). This is consistent with the sulfur
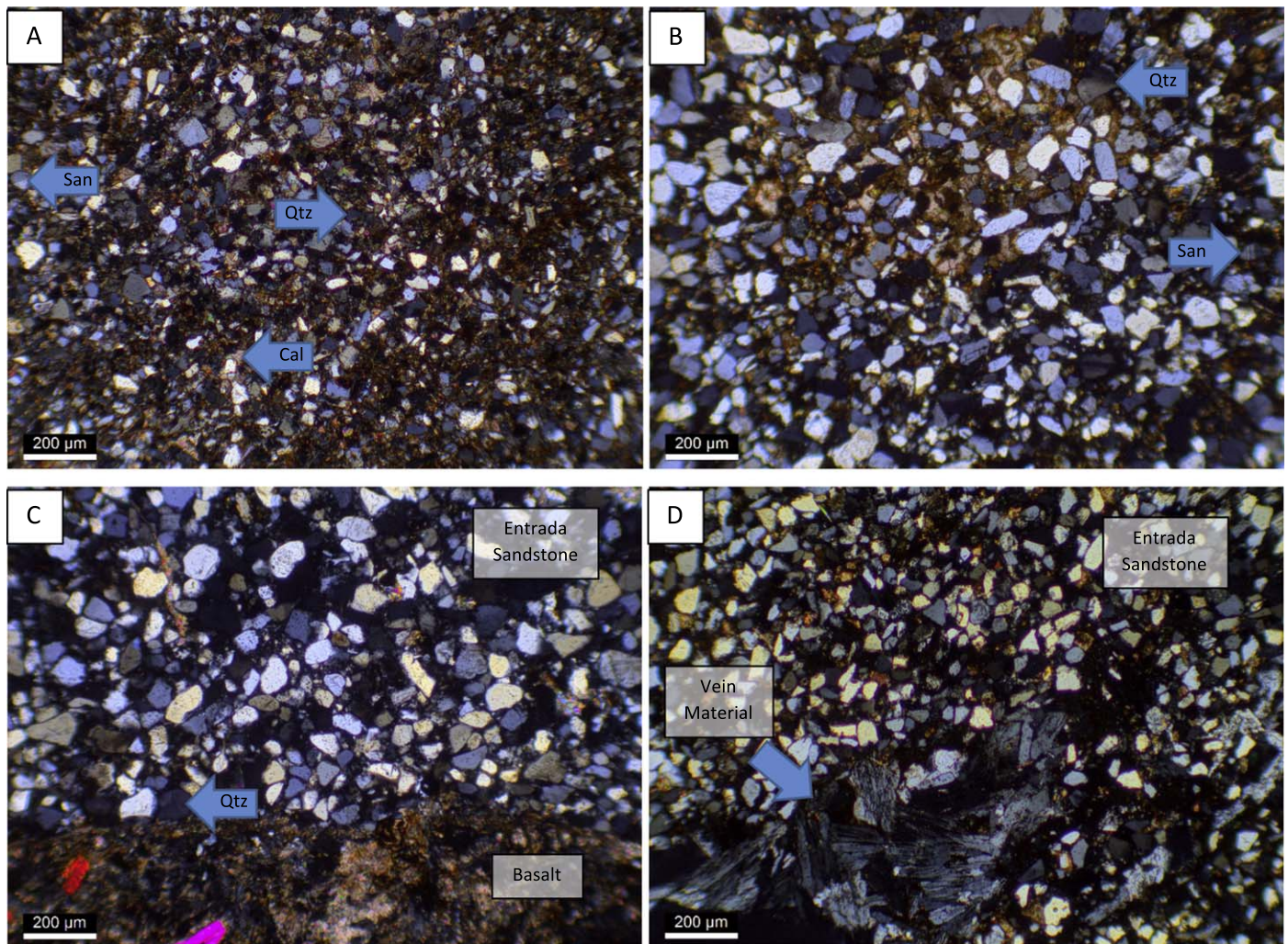
Figure 7. (a) The unaltered Entrada Sandstone (sample 34), which is dominated by quartz with sanidine and has calcite and iron-oxide cement. (b) The metamorphosed Entrada Sandstone at the contact zone (sample 2), showing quartz and sanidine but having little to no calcite or iron-oxide cement. (c) Xenolitic material (sample 27), showing a piece of the Entrada Sandstone that had been incorporated into the basalt. The basalt is shown at the bottom of the image. (d) Sample 30, which is the vein at the lower left portion of the image.

isotopic composition of the altered dike itself, which ranges from $\delta 34S = +16.1‰$ (green) to $\delta 34S = +10.5‰$ (red) (Figure 7(b)).

Altered mafic dike results. Mineralogy, geochemistry, and new isotopic data. Costello et al. (2020) showed that in the field the dike can be divided into four zones based on the extent of alteration: dark, green, purple, and red (Figure 1). Samples contain calcite, hematite, and kaolinite, with minor goethite, gypsum, and halite. The mineralogy shows an increase in sulfate and iron-oxide minerals with increasing alteration. The bulk chemistry of these four zones is consistent with fluid mobility removing Si and K but adding S, Fe, Ca, and possibly Mg as alteration progresses. New results for these same samples for S, C, and O isotopes show that even though the basalts are altered to a different extent, the isotopic results cluster for the mafic dike samples. From least to most altered, the dike had -4.8 $\delta^{13}C$, -11.9 $\delta^{18}O$, 13.3 $\delta 34S$ (16—black); -4.0 $\delta^{13}C$, -9.2 $\delta^{18}O$, 16.1 $\delta 34S$ (31—green); -4.1 $\delta^{13}C$, -13.4 $\delta^{18}O$, 15.4 $\delta 34S$ (11—purple); and -4.1 $\delta^{13}C$, -13.6 $\delta^{18}O$, 10.5 $\delta 34S$ (5—red). This shows how constant the C and O isotopes are for the altered portion of the dike, with the S isotopes still consistent but slightly more variable, having

-4.1 ± 0.1 $\delta^{13}C$, -12.1 ± 2.1 $\delta^{18}O$, 14.1 ± 3.1 $\delta 34S$ (Figure 9).

6. Discussion

Conditions of metamorphism for the xenolith. Here, we discuss the mineralogical changes recorded by the xenolith separately from the other samples. Due to the xenolith being incorporated into the dike itself (Figure 5), it should have recorded higher temperatures and potentially fewer and/or higher-salinity fluids than the rest of the system. Like all other samples, the xenolith is dominated by quartz and feldspars (Table 1; Supplemental Table 2; Crandall 2021). The minor minerals in the xenolith reveal the temperature and fluid conditions of the system. Specifically, the xenolith contains tridymite, a silica polymorph that is only stable at temperatures $>870°C$ at one bar (e.g., Deer et al. 2013). The xenolith and altered mafic dike contain abundant kaolinite, which is consistent with hydrothermal alteration of the mafic dike (Costello et al. 2020). The dike also includes a small amount of dolomite, along with a large portion of calcite. The mineralogy is consistent with high ($\gg700°C$) temperatures associated with the sandstone material in the dike as it was emplaced.
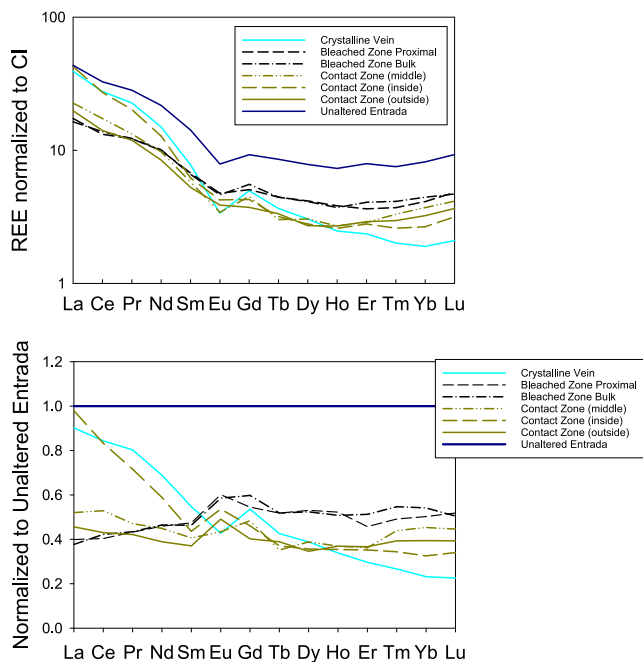
Figure 8. Top: Rare Earth Elements (REE) normalized to CI chondrites (Anders & Grevesse 1989) compared with the REE for the unaltered Entrada Sandstone. All samples are light REE enriched and have a slightly negative europium anomaly. Bottom: REE normalized to the unaltered Entrada Sandstone showing that all samples are depleted in bulk REE compared with Entrada but that most samples have similar patterns and therefore flat patterns when normalized against the unaltered sample. The exceptions are the inside of the contact zone and the crystalline vein having fractionated patterns from the unaltered with a Light REE enrichment and relatively flat mid- and heavy REE compared with the unaltered.

Figure 9. Top: $\delta^{13}C$ vs. $\delta^{18}O$ for the Entrada (star), altered Entrada (squares), and mafic dike samples (circles) from Costello et al. (2020). Samples with similar $\delta^{13}C$ values (determined by eye) are circled for comparison. Bottom: $\delta^{34}S$ vs. $\delta^{18}O$ for the same samples and same symbols as in the top panel. All samples have similar $\delta^{34}S$, except the unaltered Entrada (star) and the outside of the contact zone (yellow triangle).

Conditions of alteration. Based only on the chemical and mineralogical changes in the dike from the hydrothermal activity, Costello et al. (2020) constrained the conditions of alteration to be from a near-neutral pH fluid initially at high temperatures ($\sim$200°C). The alteration minerals in the dike itself record lower temperatures ($\geqslant$150°C) and an CO_2-bearing fluid, which evolved to a late-stage S–Cl solution (Costello et al. 2020). Using that as the basis, along with our new results, we can further constrain the evolution of the hydrothermal system.

The mineralogy of the samples, and the dominance of carbonate in all samples, suggests that the fluid would have had high CO_2 contents and been near-neutral pH (e.g., Bridges et al. 2019), similar to the conclusion from Costello et al. (2020). The carbonates are likely related to the hydrothermal activity, as they correlate with location within the system (i.e., distance from the dike) and on the similarity of the C isotopes between parts of the system most affected by fluid reactions and precipitation (Figure 9, top panel). The C isotopes are consistent between the altered dike, the contact zone, and the crystalline vein material, suggesting a similar source of the carbon in the fluid and carbonate deposition. Further, all other samples, including the bleached material and crystalline vein, have S isotopes consistent with those of the dike, suggesting that similar fluids affected all these samples.

The samples at the contact have isotopic compositions similar to the dike material, which is consistent with fluid interaction with the dike, but samples from the contact have REE patterns dissimilar from th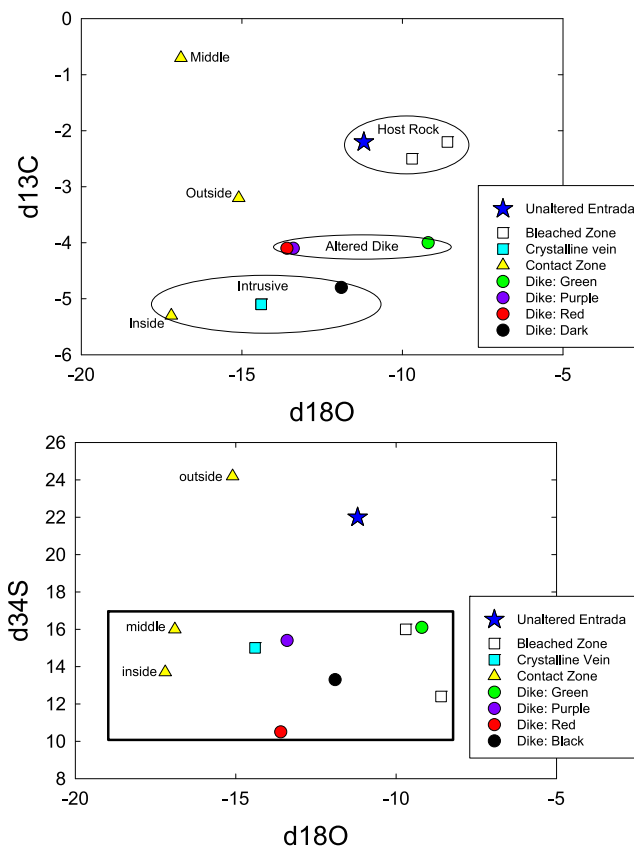e unaltered Entrada or the other altered samples. The bleached fracture samples and the samples away from the contact have similar bulk mineralogy, REE patterns, and isotopes. This is consistent with alteration under similar conditions removing REE, Fe, Al, and P from the samples, but adding Ca, K, and CO_2 (shown as LOI and carbonates in the samples).

An interesting note is that the outside of the contact zone has S isotopes consistent with the unaltered Entrada and C isotopes between that of the middle portion of the contact zone, the unaltered Entrada, and the altered dike material (Figure 9). This may suggest that it was not as extensively affected by fluid mobility or heat from the dike; however, the bulk composition (Figures 6, 8) and mineralogy are quite different from the unaltered Entrada (Table 1; Supplemental Table 2; Crandall 2021). This may be consistent with the interpretation of the middle portion data, in that there was some biomediation causing isotopic fractionation.

In the crystalline vein material, the mineralogy is different with marialite and celestine that can be used to constrain the fluid conditions. Marialite has a very restrictive range of formation conditions. Filiberto et al. (2014) previously found marialite in Martian meteorite Nakhla, and combining this previous work with new experimental results constrains this formation condition to temperatures $> 750°$ C from a Cl-rich, low water activity brine (Filiberto et al. 2014; Almeida & Jenkins 2019). (One caveat is that most alteration minerals found in Nakhla are due to lower-temperature, possibly impact-
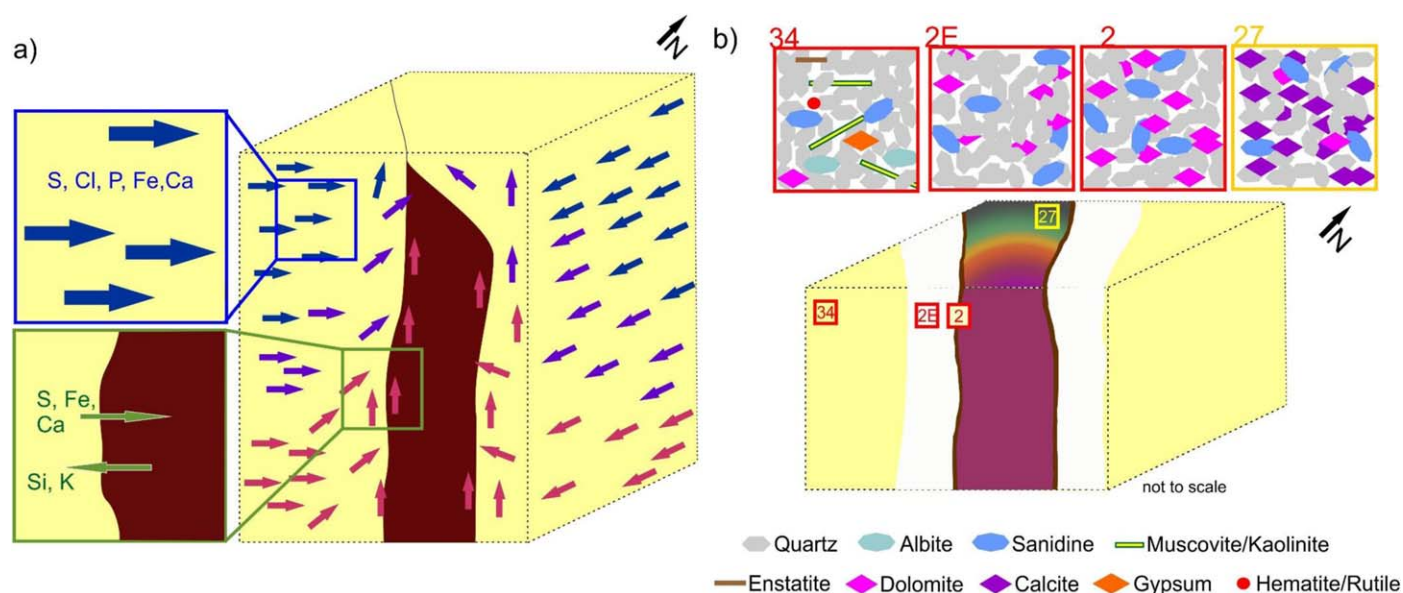
Figure 10. The hydrothermal system history (a) during and (b) after dike emplacement within the Entrada Sandstone. Figure is not to scale. (a) Intrusion of the dike into the sandstone producing a hydrothermal system circulating through the sandstone and penetrating the dike after cooling below its ductile temperature and fracture formation; green arrows indicate element mobility. Redder arrows represent hot fluids, while bluer arrows represent cold fluids. (b) The system after erosion and how it appears today. Numbers represent samples collected for analyses. Orange boxes show the representative mineralogy for samples that experienced hydrothermal alteration, while the yellow box shows the mineralogy for the xenolithic material. Modified from Costello et al. (2020) to include metamorphism and hydrothermal activity of the surrounding Entrada Sandstone.

generated, hydrothermal activity; Bridges & Schwenzer 2012; Hicks et al. 2014.) Filiberto et al. (2014) previously suggested that the marialite in Nakhla formed from a high-temperature Cl-rich fluid that, after cooling substantially, could have become a habitable environment for halophiles; however, these previous results were for marialite only. Here we have celestine as well, which forms as a product of the reaction of hypersaline Sr-bearing fluids with gypsum and/or anhydrite over a large range of temperatures and pressures (e.g., Hanor 2000). Both the bulk REE of altered samples and the presence of celestine suggest that REE were mobile in the system, and with this sample's REE patterns and isotopes similar to baked sandstone (sample 2D) in direct contact with the magmatic dike, this is suggestive of the fluids precipitating the vein material and of the contact zone being derived or at least related to the magmatic system.

Costello et al. (2020) reported a fluid up to ∼200°C, near-neutral pH, and CO_2-rich based on mineralogy throughout the dike, bulk chemical changes associated with alteration, and a comparison of the combined mineral and bulk chemical changes with geochemical models from Filiberto & Schwenzer (2013). However, the altered dike likely saw high fluid:rock ratios and therefore may not have preserved the highest temperatures of alteration. Therefore, here we combine the mineralogy, chemistry, and isotopes of the bleached zones, the contact zone, the altered dike, and the crystalline vein material, to better constrain not only the hydrothermal activity of the dike itself but also how the fluid evolved as it moved away from the dike and cooled (Figure 10). The maximum recorded temperature of the fluid would have been ∼750°C based on the presence of marialite. The baked sediments record even hotter temperatures (up to 870°C) based on tridymite, but this may not have been in contact with fluids. The fluid would have been a near-neutral pH brine based on the abundance of carbonates deposited in the system. The fluid would also have had to have high CO_2, S, and Cl activity and contain REE, Fe, P, K, Ca, and possibly Si based on the bulk chemistry and mineralogy of

the altered samples with constraints from mineral stability experimental results and geochemical models (Figure 10). This shows that the magmatic intrusion imposed a large temperature gradient of the surrounding area and disturbed the preexisting thermochemical equilibria.

Constraints on habitability. To constrain habitability of our system, we follow Perl et al. (2021) and Conrad (2014) constraints on habitable planetary environments based on terrestrial systems: temperature, pH, salinity, nutrient supply, oxygen, radiation, and pressure. For each of these constraints, we will discuss them in the context of the mineralogy and geochemistry data to show that the system would have been a habitable environment. Radiation and pressure will not be included in the discussion, since we do not have strong constraints based on the current data. However, it must be noted that although UV and cosmic radiation on the present-day surface of Mars is deemed determinantal for putative life, the denser Martian atmosphere during the Noachian would have provided protection (e.g., Molina-Cuberos et al. 2001). The highest-temperature estimate we have of the fluid (750°C) based on Marialite stability is well outside the conditions of habitability on Earth and in fact would have likely sterilized the local environment (e.g., Rothschild & Mancinelli 2001; Kashefi & Lovley 2003; Cowan 2004); however, temperature estimates range from 750°C down to nearly room temperature, based on carbonate and sulfate stability. Therefore, the hydrothermal system that formed during interaction of the magma and groundwater would have been habitable, once the system cooled below ∼120°C based on the requirements for life on Earth (e.g., Rothschild & Mancinelli 2001; Cockell et al. 2012, 2016; Conrad 2014).

The mineralogy of the samples, as well as the dominance of carbonate in all samples, suggests that the fluid would have been near-neutral pH. The fluid (as summarized in Figure 10) would have contained key bio-essential elements (e.g., C, H, N, O, P, S) and redox couples (e.g., involving Fe and S), which

could have been utilized by chemolithotrophic microorganisms to support microbial growth (Neubauer et al. 2002; Gómez et al. 2010; Westall et al. 2015; Price et al. 2018). Further, the system would have likely been an oxidizing environment based on the presence of hematite throughout the altered dike (Costello et al. 2020), which may have been sufficient to support aerobic metabolism (e.g., Stamenković et al. 2018).

The hydrothermal fluid would have likely been Cl-rich, based on the mineralogy and bulk chemistry (Costello et al. 2020), and evolved to a high Cl activity, low water activity brine as evidenced by the presence of marialite. Although this brine would have been too chlorine-rich for most terrestrial microorganisms, the fluid would have been habitable for specialized microorganisms called halophiles that can grow between 0.5 and 5.2 M NaCl (e.g., DasSarma 2006; Oren 2008; Perl & Baxter 2020), as was previously suggested for magmatic-hydrothermal alteration during the crystallization of the Nakhla meteorite (e.g., Filiberto et al. 2014). Halophiles such as *Halobacteriaceae* and *Dunaliella salina* can thrive in such Cl-rich systems (e.g., Rothschild & Mancinelli 2001; DasSarma 2006) and represent a potential analog for life that could exist within the high-Cl contents of the Martian crust (e.g., Mancinelli et al. 2004; Keller et al. 2006; Filiberto & Schwenzer 2019).

Support for habitability comes from the middle portion of the contact zone, where the sample contains dolomite instead of calcite and has a heavy carbon isotopic signature (Figure 9). The middle portion of the baked zone is mineralogically and isotopically (C and O) distinct from all other samples and is the only sample that contains significant dolomite. Further, a trend in the C isotopes of the contact zone displays an increase in the heavy fraction of C isotopes at a constant O isotopic signature in the middle portion of the baked zone (Figure 9). The combination of dolomite and the heavy C isotopes may suggest microbial activity because of two reasons: (1) the observation represents a significant increase of isotopically heavy C over a short distance, which is potentially indicative of microbes preferentially taking up the light C isotope and causing the resultant minerals to be isotopically heavy (Dupraz et al. 2009); and (2) dolomite is commonly biomediated (e.g., Roberts et al. 2004; Petrash et al. 2017). For example, methanogenic archaea, which has been suggested as a plausible metabolism for Mars (e.g., Kral et al. 2004; Morozova & Wagner 2007), generate isotopically "light" methane, leaving the remaining dissolved carbon enriched in ^{13}C and producing isotopically heaving carbonates (see review and Figure 7 in Petrash et al. 2017). Methanogenic archaea do not typically affect the oxygen isotopes of the system or the carbonates that precipitate. For comparison, authigenic carbonates typically show bulk negative carbonate signatures (e.g., Petrash et al. 2017). Further, microbially induced dolomite and calcite precipitation from altered basalt in the subsurface produce values of $\delta^{13}C = -0.59‰ \pm 0.28‰$ (Roberts et al. 2004), and these values match the dolomite-bearing middle sample of the contact zone ($\delta^{13}C = -0.7‰$), suggesting microbial activity during the hydrothermal activity. Such a relatively constant oxygen isotope with an enrichment in heavy carbon isotopes is seen in the middle portion of the baked zone in our samples, suggestive of microbial activity. However, further work on this and other samples in the area would be needed to confirm not only that the system was a habitable environment but also that

it was inhabited—and to classify what was living in the system and when.

Comparison to bleached features in other sandstones in the area. Bleaching features have been found in Jurassic sandstones on the Colorado Plateau, though caused by very different processes (e.g., Beitler et al. 2003, 2005; Parry et al. 2004; Yoshida et al. 2018), prompting an interesting comparison. Portions of the Navajo, Entrada, and Wingate sandstones likely became bleached because of infiltration of a reducing fluid into the reservoir, leading to the removal of primary iron-oxide grain coatings from the sandstones (e.g., Beitler et al. 2003; Parry et al. 2004), whereby the majority of the bleaching was associated with Laramide-age structural uplifts and monoclines (e.g., Beitler et al. 2003; Parry et al. 2004). Alternatively, iron can be mobilized as Fe^{3+} by highly acidic fluids (Yoshida et al. 2018). Similar to the mineralogy here, the bleached zones are dominated by quartz with K-feldspar and calcite. Iron is still present as minor amounts of pyrite or hematite but is less abundant than in the unbleached zones.

The main difference between the bleached zones in other fracture zones and the ones present in our field site is the nature of the fluid causing the bleaching. In other zones, the bleaching is mainly caused by hydrocarbon migration through the porous sandstone along fractures (e.g., Beitler et al. 2003; Parry et al. 2004), whereas at our site the bleaching is caused by migration of hot oxidizing hydrothermal fluids interacting with the mafic dike and fluids in the surrounding porous sandstone (Figure 10). Interestingly, both produce similar mineralogy in the bleached zones, despite rather different fluid compositions and temperatures of alteration. However, the difference in the fluid is evidenced in the crystalline vein material that fills a fracture in our bleached zone compared with the mineralogy of the other bleached fractures with our samples containing high-Cl, high-S minerals. Further, our site shows evidence for a larger-scale metamorphic and hydrothermal system that is not present at other sites with bleached fractions. We do not expect significant hydrocarbons in the crust of Mars. Instead, bleached fracture features that have been observed on Mars from orbit at Candor Chasma and in situ at Gale Crater (Okubo & McEwen 2007; Horgan et al. 2020; Stein et al. 2020) are more likely to have been formed from interaction with fluid compositions similar to those inferred from our field area (see more details below). Importantly, our field site demonstrates the importance of investigating the bleached features in context with mineralogy of the surrounding area to constrain temperatures and processes of formation.

7. Implications for Early Mars

During the Noachian, the Martian crust was a dynamic environment with both volcanism and meteorite impacts churning and modifying the crust, producing both contact metamorphism and high-temperature hydrothermal systems (e.g., Osinski et al. 2001; Abramov & Kring 2005; Pirajno & Van Kranendonk 2005; Carr & Head 2010; Schwenzer et al. 2012a; Arvidson et al. 2014; Turner et al. 2016). Such systems should have left behind evidence as remnant mineralogy or potentially bleached zones. The results here can be compared with those and used to constrain their formation history.

Haloed or light-toned material that cuts across darker bedrock has been detected both from orbit at Candor Chasma and at Gale Crater (e.g., Okubo & McEwen 2007; Stein et al. 2020).

At Candor Chasma, the light-toned halos are raised ridges against a darker bedrock material and have been suggested to represent bleaching of the bedrock with chemical precipitation of Fe-bearing minerals into pore spaces of previous fractures of the bedrock (Okubo & McEwen 2007). At Vera Rubin ridge within Gale Crater, there are light-toned materials that crosscut primary bedding (Stein et al. 2020). These are interpreted to represent remnants of diagenetic alteration after deposition of the sediments (Horgan et al. 2020). Mineralogically, Vera Rubin ridge contains plagioclase, pyroxene, hematite, Ca-sulfate minerals, phyllosilicates, with significant amounts of amorphous materials (Rampe et al. 2020a, 2020b). Interestingly, in Gale Crater tridymite was detected downslope of Vera Rubin ridge and is thought to represent evidence for silicic volcanism (Morris et al. 2016). Here, we show that high-temperature hydrothermal fluid can form both bleached features and tridymite, which suggests that such a process could similarly produce these features at Gale Crater. Such a magmatic-hydrothermal system, as shown here, would also have been a habitable environment with the timescales for habitability depending on groundwater or fluid recharge to the system. However, igneous material has only been analyzed as float rocks within Gale Crater likely brought in from a broader region (e.g., Cousin et al. 2017; Edwards et al. 2017; Siebach et al. 2017). Instead, the bleached features, along with the tridymite, could have formed from an impact-induced hydrothermal system, as would be expected in Gale Crater (Schwenzer et al. 2012a), or high-temperature hydrothermal systems along preexisting fractures (Yen et al. 2021). Impact-induced hydrothermal systems based on the size of Gale Crater could have been active for up to $\sim$300,000 yr (Abramov & Kring 2005; Schwenzer et al. 2012a); while a large time gap between the impact and the sediment deposition is likely and thus a connection between the two is unlikely, without constraints on the age of the bleached features and tridymite formation, it is hard to fully rule out either process (impact- or magmatic-induced hydrothermal systems). Such a hydrothermal system on Earth would have been a habitable environment, as indicated by recent results showing that the hydrothermal system associated with the Chicxulub impact site was habitable for a duration in excess of 10^6 yr (Kring et al. 2020).

Beyond the haloed features, ancient Mars terrain, as measured by orbital spectroscopy, has comparable mineralogy to the alteration mineralogy analyzed at our field site: carbonates associated with mafic minerals, sulfates, and kaolinite and/or other clay minerals (e.g., Ehlmann & Edwards 2014; Filiberto & Schwenzer 2019 and references within). On a side note, marialite has also been found in one melt inclusion in Nakhla (Filiberto et al. 2014), but that rock is Amazonian and not Noachian in age (Korochantseva et al. 2011). Therefore, this site is an important analog location for informing about both alteration and habitability potential of the early Martian crust, with potential implications for younger Mars.

Our work here shows that magma–sediment contacts should be targeted for study by Mars 2020 Perseverance rover in Jezero Crater. These should occur both in Jezero Crater and in the broader region of NE Syrtis, where two proposed volcanic units are directly in contact with sedimentary units—the Syrtis Major lavas in contact with layered sulfates, and the floor unit in Jezero Crater, which is proposed to be of magmatic origin and in contact with carbonate sediments (Ehlmann & Mustard 2012; Goudge et al. 2015, 2017; Salvatore et al.

2018; Horgan et al. 2020). Our results show that spectroscopic (such as MastCam-Z; Bell et al. 2021) and geomorphologic investigations should be able to pinpoint these contact zones and any bleached features for more detailed analyses. While Mars 2020 Perseverance rover does not have the ability to measure C or O isotopes (Williford et al. 2018), constraining habitability based on this Mars analog site is focused on geochemical gradients and mineralogical changes across the contact zone; therefore, PIXL (Allwood et al. 2015) and SuperCam (Wiens et al. 2012) investigations should be targeted to geochemically map such features. If the results—adjusted for the differences in host rock—show mineralogy changes and/or geochemical changes comparable to our site, the Perseverance science team should drill into a fracture-associated halo because of the possibility of a habitable environment and cache this sample for sample return. Similarly, the Panoramic Camera (PanCam), Infrared Spectrometer for ExoMars (ISEM), and Raman Laser Spectrometer (RLS) on ESA's ExoMars Rosalind Franklin rover (Vago et al. 2015) should be used for detailed investigations of magma–sediment contacts and any bleached features, and these should be drilled for detailed investigations.

8. Conclusions

Our study shows that a magmatic intrusion with its temperature gradient and disturbance of the preexisting thermochemical equilibria causes a wide range of mineral-forming environments and associated assemblages. Within each of those environments, pH and element availability vary, but most importantly, active processes are ongoing to reestablish the disturbed equilibrium. It is those disequilibrium conditions that are most favorable to be utilized by microbial life and, if conditions persisted for an extended period of time (by the standards of microbial generations), for specialized microbes to take advantage. In our analog case study, the mineralogy and geochemical changes record evidence for a habitable environment once the system cooled below $\sim$120°C, while the middle portion of the contact zone site suggests evidence for the presence of microbial activity based on the combination of dolomite and C isotopes signature. Therefore, it is paramount that future missions such as the Mars 2020 rover Perseverance and the ExoMars Rosalind Franklin rover investigate the interface of sediments with magmas or impact melts where microbial life, if present, could have taken advantage of this selection of favorable conditions. However, as our results show, finding definitive evidence of life in such samples even in terrestrial systems is not straightforward, and further analog work is needed to help constrain the ability to detect these habitable environments on Mars. It is vital that the NASA Mars 2020 Perseverance rover and the ESA ExoMars Rosalind Franklin rover teams conduct detailed geochemical and mineralogical investigations of any magma–sediment contact and associated bleached features because they may represent habitable environments. If any of these sites have comparable mineralogy and geochemical gradients to those observed here, it is vital to cache these samples with similar alteration mineralogy to our site and return these for in-depth analyses.

ORCID iDs

Jake R. Crandall ⓘ https://orcid.org/0000-0003-0790-9885
Justin Filiberto ⓘ https://orcid.org/0000-0001-5058-1905
Susanne P. Schwenzer ⓘ https://orcid.org/0000-0002-9608-0759

References

Abramov, O., & Kring, D. A. 2005, JGRA, 110, E12S09
Abramov, O., & Kring, D. A. 2007, M&PS, 42, 93
Allwood, A., Clark, B., Flannery, D., et al. 2015, in 2015 IEEE Aerospace Conf. (Piscataway, NJ: IEEE), 1
Almeida, K. M., & Jenkins, D. M. 2019, AmMin, 104, 1788
Anders, E., & Grevesse, N. 1989, GeCoA, 53, 197
Andrews-Hanna, J. C., Zuber, M. T., & Banerdt, W. B. 2008, Natur, 453, 1212
Arvidson, R. E., Squyres, S. W., Bell, J. F., et al. 2014, Sci, 343, 1248097
Baharier, B., Semprich, J., Olsson-Francis, K., et al. 2021, LPSC, 52, 1284
Beitler, B., Chan, M. A., & Parry, W. T. 2003, Geo, 31, 1041
Beitler, B., Parry, W., & Chan, M. A. 2005, JSedR, 75, 547
Bell, J., Maki, J., Mehall, G., et al. 2021, SSRv, 217, 24
Bibring, J.-P., Langevin, Y., Mustard, J. F., et al. 2006, Sci, 312, 400
Bridges, J. C., Hicks, L. J., & Treiman, A. H. 2019, in Volatiles in the Martian Crust, ed. J. Filiberto & S. P. Schwenzer (Amsterdam: Elsevier), 89
Bridges, J. C., & Schwenzer, S. P. 2012, E&PSL, 359, 117
Carr, M. H. 1980, AmSci, 68, 626
Carr, M. H., & Head, J. W. 2003, JGRE, 108, 5042
Carr, M. H., & Head, J. W. 2010, E&PSL, 294, 185
Chan, M. A., Beitler, B., Parry, W., Ormö, J., & Komatsu, G. 2004, Natur, 429, 731
Cheng, Z., Fernández-Remolar, D. C., Izawa, M. R. M., et al. 2016, JGRG, 121, 1593
Clifford, S. M., & Parker, T. J. 2001, Icar, 154, 40
Cockell, C. S. 2006, RSPTB, 361, 1845
Cockell, C. S., Balme, M., Bridges, J. C., Davila, A., & Schwenzer, S. P. 2012, Icar, 217, 184
Cockell, C. S., Bush, T., Bryce, C., et al. 2016, AsBio, 16, 89
Conrad, P. G. 2014, Sci, 346, 1288
Costello, L., Filiberto, J., Crandall, J., et al. 2020, Geoch, 80, 125613
Cousin, A., Sautter, iolaine, Payré, V., et al. 2017, Icar, 288, 265
Cowan, D. A. 2004, Trends in Microbiology, 12, 58
Crabaugh, M., & Kocurek, G. 1993, GSLSP, 72, 103
Crandall, J. R. 2021, PhD thesis, Southern Illnois Univ. Carbondale
Crandall, J. R., Filiberto, J., Potter-McIntyre, S., & Schwenzer, S. P. 2021, AmMin, submitted
DasSarma, S. 2006, Microbe-American Society for Microbiology, 1, 120
Deer, W. A., FRS, Howie, R. A., & Zussman, J. 2013, Silica Minerals: Quartz, An Introduction to the Rock-Forming Minerals (Hoboken, NJ: Prentice Hall)
Dupraz, C., Reid, R. P., Braissant, O., et al. 2009, ESRv, 96, 141
Edwards, P. H., Bridges, J. C., Wiens, R., et al. 2017, M&PS, 52, 2931
Ehlmann, B. L., & Edwards, C. S. 2014, AREPS, 42, 291
Ehlmann, B. L., & Mustard, J. F. 2012, GeoRL, 39, L11202
Ehlmann, B. L., Mustard, J. F., Clark, R. N., Swayze, G. A., & Murchie, S. L. 2011, CCM, 59, 359
Farmer, J. D. 1996, Ciba Foundation Symp. (New York: Wiley), 273
Filiberto, J. 2017, ChGeo, 466, 1
Filiberto, J., McCubbin, F. M., & Taylor, G. J. 2019, in Chapter 2 in Volatiles in the Martian Crust, ed. J. Filiberto & S. P. Schwenzer (Amsterdam: Elsevier), 13

Filiberto, J., & Schwenzer, S. P. 2013, M&PS, 48, 1937
Filiberto, J., & Schwenzer, S. P. 2019, Volatiles in the Martian Crust (Amsterdam: Elsevier), 426
Filiberto, J., Treiman, A. H., Giesting, P. A., Goodrich, C. A., & Gross, J. 2014, E&PSL, 401, 110
Gómez, F., Mateo-Martí, E., Prieto-Ballesteros, O., Martín-Gago, J., & Amils, R. 2010, Icar, 209, 482
Goudge, T. A., Milliken, R. E., Head, J. W., Mustard, J. F., & Fassett, C. I. 2017, E&PSL, 458, 357
Goudge, T. A., Mustard, J. F., Head, J. W., Fassett, C. I., & Wiseman, S. M. 2015, JGRE, 120, 775
Griffiths, R. W. 2000, AnRFM, 32, 477
Hanor, J. S. 2000, RvMG, 40, 193
Hicks, L. J., Bridges, J. C., & Gurman, S. J. 2014, GeCoA, 136, 194
Hochstein, M., & Browne, P. 2000, Encyclopedia of Volcanoes (Amsterdam: Elsevier), 835
Horgan, B. H. N., Johnson, J. R., Fraeman, A. A., et al. 2020, JGRE, 125, e06322
Jakosky, B. M., & Phillips, R. J. 2001, Natur, 412, 237
Kashefi, K., & Lovley, D. R. 2003, Sci, 301, 934
Keller, J. M., Boynton, W. V., Karunatillake, S., et al. 2006, JGRE, 111, E03S08
Korochantseva, E. V., Schwenzer, S. P., Buikin, A. I., et al. 2011, M&PS, 46, 1397
Kostka, J. E., Dalton, D. D., Skelton, H., Dollhopf, S., & Stucki, J. W. 2002, ApEnM, 68, 6256
Kral, T. A., Bekkum, C. R., & McKay, C. P. 2004, OLEB, 34, 615
Kring, D. A., Tikoo, S. M., Schmieder, M., et al. 2020, SciA, 6, eaaz3053
Lasue, J., Clifford, S. M., Conway, S. J., Mangold, N., & Butcher, F. E. G. 2019, in Volatiles in the Martian Crust, ed. J. Filiberto & S. P. Schwenzer (Amsterdam: Elsevier), 185
Leone, G. 2020, E&PS, 7, e2019EA001031
Malin, M. C., & Edgett, K. S. 1999, GeoRL, 26, 3049
Mancinelli, R. L., Fahlen, T. F., Landheim, R., & Klovstad, M. R. 2004, AdSpR, 33, 1244
McSween, H. Y., Grove, T. L., & Wyatt, M. B. 2003, JGRE, 108, 5135
McSween, H. Y., Labotka, T. C., & Viviano-Beck, C. E. 2015, M&PS, 50, 590
McSween, H. Y., Taylor, G. J., & Wyatt, M. B. 2009, Sci, 324, 736
McSween, H. Y., & Treiman, A. H. 1998, in Martian Meteorites, Reviews in Mineralogy, ed. J. J. Papike (McLean, Va: Mineralogical Society of America)
Melchiorre, E. B., Sickman, J. O., Talyn, B. C., & Noblet, J. 2018, JArEn, 148, 45
Milliken, R. E., Swayze, G. A., Arvidson, R. E., et al. 2008, Geo, 36, 847
Molina-Cuberos, G. J., Stumptner, W., Lammer, H., & Komle, N. I. 2001, Icar, 154, 216
Morozova, D., & Wagner, D. 2007, FEMS Microbiol Ecol, 61, 16
Morris, Richard V., Vaniman, David T., Blake, David F., Gellert, Ralf, et al. 2016, PNAS, 113, 7071
Neubauer, S. C., Emerson, D., & Megonigal, J. P. 2002, ApEnM, 68, 3988
Newsom, H. E. 1980, Icar, 44, 207
Nisbet, E., & Sleep, N. 2001, Natur, 409, 1083
Nixon, S. L., Cockell, C. S., & Tranter, M. 2012, P&SS, 72, 116
O'Sullivan, A. 1981, in New Mexico Geological Society 32nd Annual Fall Field Conf. Guidebook, ed. R. C. Epis & J. F. Callender (Socorro, NM: New Mexico Geological Society), 89, https://nmgs.nmt.edu/publications/guidebooks/downloads/32/32_p0089_p0096.pdf
Okubo, C. H., & McEwen, A. S. 2007, Sci, 315, 983
Oren, A. 2008, Saline Systems, 4, doi:10.1186/1746-1448-4-2
Osinski, G. R., Spray, J. G., & Lee, P. 2001, M&PS, 36, 731
Osinski, G. R., Tornabene, L. L., Banerjee, N. R., et al. 2013, Icar, 224, 347
Parry, W., Chan, M. A., & Beitler, B. 2004, AAPG Bulletin, 88, 175
Perl, S. M., & Baxter, B. K. 2020, in Great Salt Lake: Biology of a Terminal Lake in the Age of Change, ed. B. K. Baxter & J. Butler (Cham: Springer) doi:10.1007/978-3-030-40352-2_16
Perl, S. M., Celestian, A. J., Cockell, C. S., et al. 2021, AsBio, in press
Petrash, D. A., Bialik, O. M., Bontognali, T. R. R., et al. 2017, ESRv, 171, 558
Pirajno, F., & Van Kranendonk, M. 2005, AuJES, 52, 329
Potter, S. L., & Chan, M. A. 2011, Geofluids, 11, 184
Price, A., Pearson, V. K., Schwenzer, S. P., Miot, J., & Olsson-Francis, K. 2018, Frontiers in Microbiology, 9, 513
Rampe, E., Bristow, T., Morris, R., et al. 2020a, LPSC, 51, 1601
Rampe, E. B., Blake, D. F., Bristow, T. F., et al. 2020b, Geoch, 125605
Rampe, E. B., Ming, D. W., Blake, D. F., et al. 2017, E&PSL, 471, 172
Roberts, J. A., Bennett, P. C., Gonzaález, L. A., Macpherson, G. L., & Milliken, K. L. 2004, Geo, 32, 277

Rodríguez, A., & Van Bergen, M. 2016, Netherlands Journal of Geosciences, 95, 153

Rogers, A. D., Warner, N. H., Golombek, M. P., Head, J. W., III, & Cowart, J. C. 2018, GeoRL, 45, 1767

Rothschild, L. J., & Mancinelli, R. L. 2001, Natur, 409, 1092

Ruff, S. W., Campbell, K. A., Van Kranendonk, M. J., Rice, M. S., & Farmer, J. D. 2020, AsBio, 20, 475

Ruff, S. W., & Farmer, J. D. 2016, NatCo, 7, 13554

Ruff, S. W., Farmer, J. D., Calvin, W. M., et al. 2011, JGRE, 116, E00F23

Salvatore, M. R., Goudge, T. A., Bramble, M. S., et al. 2018, Icar, 301, 76

Sapers, H., Osinski, G., & Banerjee, N. 2009, AGUSM, B13B-10

Schmidt, M. E., Campbell, J. L., Gellert, R., et al. 2014, JGRE, 119, 64

Schröder, C., & Schwenzer, S. P. 2017, LPSC, 48, 2429

Schulze-Makuch, D., Dohm, J. M., Fan, C., et al. 2007, Icar, 189, 308

Schwenzer, S. P., Abramov, O., Allen, C. C., et al. 2012a, E&PSL, 335, 9

Schwenzer, S. P., Abramov, O., Allen, C. C., et al. 2012b, P&SS, 70, 84

Schwenzer, S. P., & Kring, D. A. 2013, Icar, 226, 487

Semprich, J., Schwenzer, S. P., Treiman, A. H., & Filiberto, J. 2019, JGRE, 124, 681

Shock, E. L. 1996, in Evolution of Hydrothermal Ecosystems on Earth (and Mars?), ed. G. R. Bock & J. A. Goode, Vol. 202 (New York: Wiley), 40

Shock, E. L., McCollom, T., & Schulte, M. D. 1998, Thermophiles (Boca Raton, FL: CRC Press), 79

Siebach, K. L., Baker, M. B., Grotzinger, J. P., et al. 2017, JGRE, 122, 295

Skok, J., Mustard, J., Ehlmann, B., Milliken, R., & Murchie, S. 2010, NatGe, 3, 838

Squyres, S. W., Arvidson, R. E., Ruff, S., et al. 2008, Sci, 320, 1063

Stamenković, V., Ward, L. M., Mischna, M., & Fischer, W. W. 2018, NatGe, 11, 905

Stanley, S., Elkins-Tanton, L., Zuber, M. T., & Parmentier, E. M. 2008, Sci, 321, 1822

Stein, N. T., Quinn, D. P., Grotzinger, J. P., et al. 2020, JGRE, 125, e06298

Stern, J. C., Sutter, B., Freissinet, C., et al. 2015, PNAS, 112, 4245

Strom, R. G., Croft, S. K., & Barlow, N. G. 1992, Mars (A93-27852 09-91), 383

Taylor, G. J., Boynton, W. V., Brückner, J., et al. 2006, JGRE, 111, E03S10

Taylor, G. J., Martel, L. M. V., Karunatillake, S., Gasnault, O., & Boynton, W. V. 2010, Geo, 38, 183

Taylor, S. R., & McLennan, S. M. 2009, Planetary Crusts: Their Composition, Origin and Evolution (Cambridge: Cambridge Univ. Press)

Thollot, P., Mangold, N., Ansan, V., et al. 2012, JGRE, 117, E00J06

Turner, S. M., Bridges, J. C., Grebby, S., & Ehlmann, B. L. 2016, JGRE, 121, 608

Udry, A., Howarth, G. H., Herd, C. D. K., et al. 2020, JGRE, 125, e2020JE006523

Vago, J., Witasse, O., Svedhem, H., et al. 2015, SoSyR, 49, 518

Viviano, C. E., Moersch, J. E., & McSween, H. Y. 2013, JGRE, 118, 1858

Wannamaker, P. E., Hulen, J. B., & Heizler, M. T. 2000, JVGR, 96, 175

Westall, F., Foucher, F., Bost, N., et al. 2015, AsBio, 15, 998

Wiens, R. C., Maurice, S., & Barraclough, B. 2012, SSRv, 170, 167

Williams, R. M. E., Grotzinger, J. P., Dietrich, W. E., et al. 2013, Sci, 340, 1068

Williford, K. H., Farley, K. A., Stack, K. M., et al. 2018, From Habitability to Life on Mars (Amsterdam: Elsevier), 275

Wilson, L., & Head, J. W., III 1994, RvGeo, 32, 221

Wright, J., Dickey, D., Snyder, R., Craig, L., & Cadigan, R. 1979, Measured stratigraphic sections of Jurassic San Rafael Group and adjacent rocks in Emery and Sevier Counties. Utah: US Geological Survey Open-File Report 79-1317

Yen, A. S., Morris, R. V., Clark, B. C., et al. 2008, JGRE, 111, E06S10

Yen, A. S., Morris, R. V., Ming, D. W., et al. 2021, JGRE, 126, e2020JE006569

Yoshida, H., Hasegawa, H., Katsuta, N., et al. 2018, SciA, 4, eaau0872

Zolotov, M. Y., & Mironenko, M. V. 2007, JGRE, 112, E07006